SCIENCE CHINA
Information Sciences

• **RESEARCH PAPER** •

August 2025, Vol. 68, Iss. 8, 182304:1–182304:13
https://doi.org/10.1007/s11432-024-4315-2

Co-channel multiplexing for Rayleigh-scattering-based information systems

Anchi WAN[1], Yingqing WU[1], Shibo ZHANG[1], Zhenyu YE[1], Yongxin LIANG[1], Siyuan PENG[1], Ke LIU[1], Ziwen DENG[1], Han WU[2] & Zinan WANG[1*]

[1]*Key Laboratory of Optical Fiber Sensing and Communications, University of Electronic Science and Technology of China, Chengdu 611731, China*
[2]*School of Electronics and Information Engineering, Sichuan University, Chengdu 610064, China*

Received 17 October 2024/Revised 21 January 2025/Accepted 18 February 2025/Published online 10 July 2025

Abstract A Rayleigh-scattering-based information system (RSIS) processes and conveys information by utilizing Rayleigh scattering, where the probe wave scatters off particles or molecules smaller than its wavelength, often in the context of fiber optics or atmospheric optics, etc. Wide response bandwidth is crucial for high-performance RSISs, yet it is typically constrained by the probe signal's scan rate, creating a trade-off with detection range and other key parameters. Traditional methods address this by channel multiplexing across distinct frequency bands, which increases available frequency resource consumption. Here, we introduce a co-channel multiplexing technique that significantly expands response bandwidth without requiring additional frequency resources. Central to this approach is the design of orthogonal coded sequences as the probing signal, which are then decoded using dedicatedly-designed mismatched filters. Applied to a Rayleigh-scattering-based distributed acoustic sensing (DAS) system, our method significantly broadens the response bandwidth and amplifies the signal-to-noise ratio (SNR). Experimental results corroborate the theoretical advancements, demonstrating the multiplexing of multiple co-channels and validating the system's sensing capabilities. This unveils frequency resource utilization and sets the stage for next-generation sensing technologies that demand broadband detection capabilities.

Keywords co-channel multiplexing, response bandwidth, optical pulse coding, mismatched filtering, distributed acoustic sensing, Rayleigh-scattering-based information system

Citation Wan A C, Wu Y Q, Zhang S B, et al. Co-channel multiplexing for Rayleigh-scattering-based information systems. Sci China Inf Sci, 2025, 68(8): 182304, https://doi.org/10.1007/s11432-024-4315-2

1 Introduction

The Rayleigh scattering phenomenon, where light is scattered by particles within a medium, is a cornerstone of various scientific disciplines, ranging from atmospheric science to communication theories. Rayleigh-scattering-based information systems (RSISs) exploit this effect to extract valuable information, finding applications in fields such as remote sensing [1, 2], atmospheric lidar [3], wireless communications [4], fiber-optic computing [5], random fiber lasers [6], and distributed acoustic sensing (DAS) [7]. Among these, DAS is a particularly prominent application of RSISs, leveraging the ubiquitous single-mode optical fiber (SMF) as sensing elements, capitalizing on the intrinsic Rayleigh backscattering (RBS) to sensitively and swiftly detect changes in the external environment. The swift response and exceptional sensitivity of DAS have garnered significant attention in recent years, as evidenced by its burgeoning role in seismic and oceanic movement detection [8], monitoring of glacier activities [9], structural health assessments [10, 11], or even for studying replica symmetry breaking inside fiber lasers [12].

Currently, achieving a wider response bandwidth over a longer distance for DAS has become a focal point of the domain. Yet, akin to other RSISs, DAS confronts the challenge of balancing sensing range with response bandwidth. Due to the limitation of the Nyquist sampling theorem, the response bandwidth of traditional DAS is half of the scan rate, which is the inverse of the probe pulse's repetition time. In traditional single-pulse DAS, each repetition period involves the emission of a single pulse, and the period is slightly longer than the round-trip time of lightwave traveling through the fiber to prevent overlapping RBS signals. Consequently, as the sensing distance and the round-trip time increase, the

* Corresponding author (email: znwang@uestc.edu.cn)

scan rate decreases, limiting the extension of the response bandwidth. Breaking the upper limit of the scan rate is crucial for remote DAS. In recent years, various efforts have been made to tackle this challenge from different perspectives. One approach involves leveraging hybrid sensing systems to improve detection frequency, such as combining phase-sensitive optical time-domain reflectometry (Φ-OTDR) with a Mach-Zehnder interferometer (MZI) [13, 14]. However, the complex structure increases the cost and complexity of the sensing system. Another approach focuses on using compressed sensing techniques at the signal processing end, but has a limited impact on bandwidth enhancement and is primarily suited for detecting single-frequency [15] or narrowband continuous signals [16]. Moreover, channel multiplexing techniques have been explored, which also contribute to broadening the response bandwidth and feature simple optical structures. In 2015, a temporally sequenced multi-frequency (TSMF)-source-based Φ-OTDR was proposed [17]. Later, frequency-division multiplexing (FDM) was introduced into time-gated digital optical frequency domain reflectometry (TGD-OFDR) [18]. This scheme consecutively injected linear frequency modulated (LFM) pulses of varying frequency bands into the fiber under test (FUT), employing matched filtering (MF) to discriminate overlapped signals and eliminate the inter-channel crosstalk (ICC). In 2018, instead of using a rectangular pulse, a raised-cosine-shaped pulse was employed to suppress crosstalk in an FDM-based direct detection Φ-OTDR [19]. Subsequently, the negative frequency band (NFB) has been utilized in [20], proposing a combined scheme of positive and negative multiplexing (PNM) Φ-OTDR and FDM. Nevertheless, these methods of channel multiplexing require distinct frequency bands, and the available frequency resource within a system is typically limited, necessitating prudent allocation. Therefore, achieving channel multiplexing within the same frequency band, known as co-channel multiplexing (CCM), is crucial for maximizing frequency resource utilization, which underscores its profound significance in the field.

The orthogonal coding multiplexing (OCM) technology, which is used in radar [21, 22] to implement multiple-input-multiple-output (MIMO), has recently been applied to probe pulses in optical fiber sensing systems as a novel optical pulse coding (OPC) scheme that enables CCM. OCM technology works by setting orthogonal polyphase codes within the [0, 2π] range as the initial phase of carrier signals, all operating within the same frequency band. In 2021, OCM technology was first introduced into quasi-distributed acoustic sensing (QDAS) [23]. The QDAS sensing medium utilizes optical fibers embedded with ultra-weak fiber Bragg gratings (UWFBGs) or scattering enhanced points (SEPs). This configuration ensures that the resulting sensing signals are reflection-based and inherently resistant to fading, as shown in Figure 1(a). Subsequently, the research group adjusted the constraints of orthogonal codes and generated orthogonal polyphase codes with a higher suppression ratio [24], thus increasing the response bandwidth to twenty times that of traditional single-pulse QDAS [25]. However, unlike the case in QDAS, the RBS signals in Rayleigh-scattering-based DAS systems result from the interference among scattering signals from various points, as illustrated in Figure 1(b) [26]. Consequently, these RBS signals often exhibit fading points that are randomly distributed in both location and number. It is worth noting that, the fading of RBS deteriorates coding orthogonality and leads to a significant increase in the ICC, which fundamentally impedes the implementation of OCM in DAS.

In this study, we propose a novel CCM scheme that effectively distinguishing and multiplexing aliased signals within the same frequency channel to multiply the system response bandwidth. This enables, for the first time to the best of our knowledge, overcoming the bandwidth limitations in RSISs without additional frequency allocations and any hardware extensions. Without loss of generality, we exemplify this method in the classical Rayleigh-scattering-based DAS, realizing a CCM-DAS system. Compared to traditional DAS systems, the proposed approach significantly amplifies the response bandwidth and enhances the signal-to-noise ratio (SNR), offering unprecedented advancements over traditional sensing methodologies. We meticulously crafted orthogonal polyphase codes, which are ingeniously embedded as the initial phase in the phase carrier. This strategic design engenders an orthogonal pulse sequence, setting the stage for our sophisticated decoding strategy. The proof-of-concept experiments showcase the successful multiplexing of three co-channels using three sets of orthogonal codes. Importantly, the enhancement comes without the need for additional frequency resources, underscoring the method's comprehensive sensing prowess. Moreover, the adaptability of our approach is highlighted by its potential for straightforward application to any classical scattering-based sensing systems, opens new horizons for the future of broadband signal-detection applications.

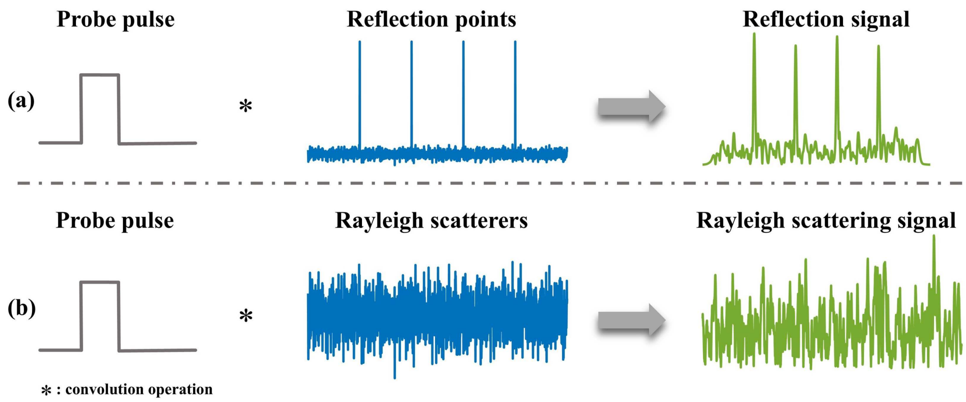

Figure 1 (Color online) Signal characteristics of reflection-based and RSISs. (a) In a reflection-based system with enhanced reflection points within the medium, the primary information originates from the areas surrounding these reflection points. The sensing medium of the QDAS system is an SMF embedded with UWFBGs/SEPs, resulting in stable reflection signals with high SNR and immunity to fading phenomena [23]. (b) In a Rayleigh-scattering-based system, where only randomly distributed micro-scatterers are present, the information is derived from the vector summation of the scattering signals. Variations in attenuation, delay, and phase shift among scattering signals from different points cause interference, leading to random fading of the signal. Consequently, in DAS systems that utilize only SMF, the obtained RBS signals are prone to distortion due to fading, ultimately degrading the sensing performance [26].

2 Principles

2.1 Principle of the proposed CCM-DAS

CCM refers to the technique of multiplexing channels that are all within the same frequency band, to maximize frequency resource utilization. Figure 2 depicts a conceptual diagram of the probe pulses in CCM-DAS. Within a repetition period of T_{rep}, M groups of pulses are injected into the FUT at equal intervals in chronological order, each group occupying the identical frequency band. The interval time between two adjacent pulses is T_{rep}/M. By leveraging the orthogonality between the backscattering signals of different probe pulses, M groups of independent sensing signals are generated. These signals are then interwoven at the signal-processing end in accordance with the temporal sequence of the injected pulse. This effectively enables M-time independent detections within a single repetition period on the fiber, thereby increasing the scan rate and enhancing the response bandwidth by a factor of M. However, achieving CCM-DAS poses the following challenges: the intervals between adjacent pulses are shorter than the round-trip time of light in the optical fiber, leading to partial overlap of RBS signals, which worsens as the number of multiplexed channels increases. In FDM-based DAS, distinguishing overlapped signals is possible by utilizing the low correlation of RBS traces from pulses with wider frequency intervals [18]. Nevertheless, in a CCM scheme, the highly correlated RBS traces at the same frequency hinder the distinction of overlapped signals. This results in significant ICC after multiplexing, leading to false vibration signals and distortion in the vibration waveform.

In this work, the OCM technique is introduced in DAS to achieve CCM by leveraging the orthogonality between the coded pulses to distinguish overlapping RBS signals. In the DAS system, the coded RBS trace can be expressed as $E(t) = h(t) * m(t)$, where $*$ denotes the convolution operation, $h(t)$ is the impulse response function of the fiber channel, and $m(t)$ is the modulated coded pulse sequence. At the demodulation part, the decoded RBS trace can be expressed as $E'(t) = E(t) \otimes m_{\mathrm{d}}(t)$, where $\otimes$ means the correlation operation, and $m_{\mathrm{d}}(t)$ is the decoding sequences.

In the orthogonal coding scheme, M sets of orthogonal polyphase codes are used, generated by the method proposed by our research group in [24] each with N-bit length. Each code is a non-return-to-zero code with each bit maintaining the same amplitude and having a phase range from 0 to 2π. The i-th modulated pulse sequence can be written as $m^i(t) = f(t) * p^i(t)$, where $f(t)$ is the phase-carrier pulse, and $p^i(t)$ is the i-th coding sequence which can be expressed as

$$p^i(t) = \sum_{k=1}^{N} \left[\exp\left[\mathrm{j}\phi_o^i(k) \right] \cdot \delta(t - (k-1)T_{\mathrm{d}}) \right], \quad k = 1, 2, \ldots, N, \tag{1}$$

where $\phi_o^i(k)$ is the element of i-th orthogonal code, and T_{d} is the duration of $f(t)$. It should be noted

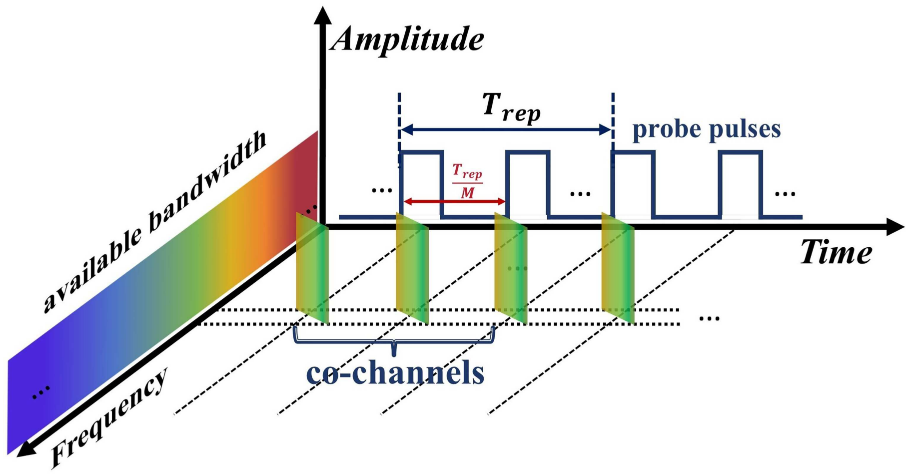

Figure 2 (Color online) Schematic concept of the probe pulses in CCM-DAS. The probe pulses in the DAS system are modulated signals generated by a modulator before entering the optical fiber. The time interval between two adjacent probe pulses, $T_{\rm rep}$, also known as the repetition period, is typically longer than the fiber length to avoid signal aliasing. In a traditional single-pulse DAS system, there is only one probe pulse within a $T_{\rm rep}$, meaning only one channel of sensing information is obtained. However, in the CCM-DAS system, M groups of pulses are present within one $T_{\rm rep}$, allowing for the acquisition of information from M channels in a single measurement period. These probe pulses are identical in amplitude and equally spaced by $T_{\rm rep}/M$ in the time domain. Moreover, each group of pulses occupies the same frequency band, which is only a small portion of the system's available bandwidth. We refer to the channels corresponding to these M groups of pulses as co-channels. At the signal processing end, these M co-channels are multiplexed through a channel interleaving technique, thereby realizing CCM-DAS. The sensing process of CCM-DAS is detailed in Figure 3.

that $f(t)$ is an LFM pulse with initial frequency f_0 and chirp rate k_s, which can be expressed as $f(t) = \exp(\mathrm{j}2\pi f_0 t + \mathrm{j}\pi k_s t^2)\cdot \mathrm{rect}(t/T_{\rm d})$. Then, M sets of coded pulse sequence can be stated as

$$m(t) = \sum_{i=1}^{M} m^i\left(t - iT_{\rm rep}/M\right) = \exp(\mathrm{j}2\pi f_0 t + \mathrm{j}\pi k_s t^2) * \sum_{i=1}^{M} p^i(t - iT_{\rm rep}/M), \quad i = 1, 2, \ldots, M, \tag{2}$$

where $T_{\rm rep}$ represents the repetition time of the probe pulse. Figure 3 depicts a conceptual schematic of CCM-DAS. As a conceptual illustration, Figure 3(a) shows the process of loading two sets of 20-bit orthogonal polyphase codes onto $f(t)$, modulating them into a coded pulse sequence $m(t)$. The different colored curves in $m(t)$ represent LFM pulses with different initial phases within the same frequency band. Subsequently, the probe pulse loaded with $m(t)$ is pumped into the FUT depicted in Figure 3(b), convolved with $h(t)$, resulting in the coded RBS trace $E(t)$:

$$E(t) = h(t) * m(t) = h(t) * \sum_{i=1}^{M} m^i\left(t - iT_{\rm rep}/M\right). \tag{3}$$

As shown in Figure 3, there are overlaps between RBS traces (more details about overlaps can be seen in Figure A1 of Appendix A), which need to be addressed. In the decoding process, the i-th code's decoder $m_{\rm d}^i(t)$ with L-bit length is expressed as

$$m_{\rm d}^i(t) = f(t) * \sum_{k=1}^{L}\Big[u^i(k)\cdot \delta(t-(k-1)T_{\rm d})\Big], \quad k = 1, 2, \ldots, L, \tag{4}$$

where $u^i(k)$ is the k-th element of i-th decoder. Then, the decoded RBS trace can be expressed as

$$E'(t,i) = h(t) * m_{\rm dp}(t,i), \tag{5}$$

where $m_{\rm dp}(t,i)$ is defined as the i-th decoded pulse sequence, which can be denoted as

$$\begin{aligned} m_{\rm dp}(t,i) &= \sum_{i=1}^{M} m^i(t - iT_{\rm rep}/M) \otimes m_{\rm d}^i(t) \\ &= m^i(t - iT_{\rm rep}/M) \otimes m_{\rm d}^i(t) + \sum_{j=1\ldots M, j\neq i}^{M} m^j(t - jT_{\rm rep}/M) \otimes m_{\rm d}^i(t). \end{aligned} \tag{6}$$

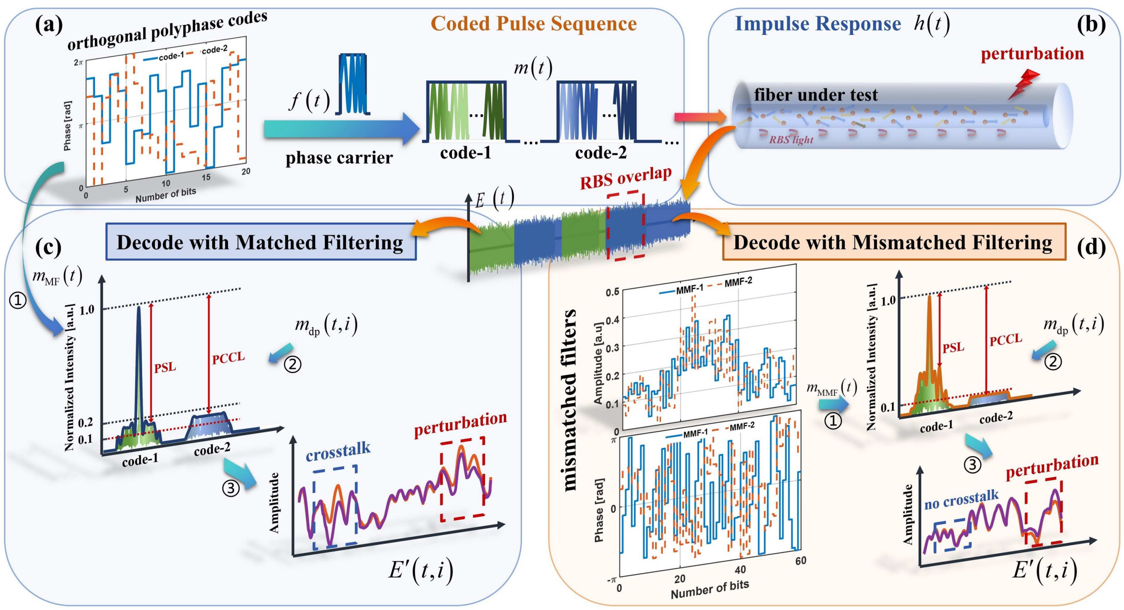

Figure 3 (Color online) Schematic concept of the CCM-DAS. (a) The phases of two 20-bit orthogonal polyphase codes are shown, with the blue solid line for code-1 and the orange dashed line for code-2, both varying from 0 to 2π. These codes are then used as initial phases on the same LFM carrier pulse $f(t)$, forming a coded pulse sequence $m(t)$. In $m(t)$, different colors and intensities indicate the sub-pulses and their initial phases. (b) The probe pulse $m(t)$, injected into the FUT, generates Rayleigh backscattering signals $E(t)$ after interacting with the fiber's scattering points. $E(t)$ is the convolution of $m(t)$ with the fiber response $h(t)$. In $E(t)$, the overlapping colored signals represent the aliasing of Rayleigh scattering signals. (c) The conventional decoding scheme uses MF. ① The orthogonal polyphase codes serve as the decoding sequence $m_{\mathrm{MF}}(t)$, cross-correlating with $m(t)$ to yield PSL and PCCL values. ② Decoding of the i-th code group produces $m_{\mathrm{dp}}(t,i)$. Convolution of $m_{\mathrm{dp}}(t,i)$ with $h(t)$ gives the decoded sensing signal. If the signal curves overlap, there is no perturbation; if they deviate, perturbation is present. ③ The curve shift at the perturbation location and crosstalk are shown. (d) The decoding with MMF is demonstrated. ① Designed mismatched filters are used as the decoding codes $m_{\mathrm{MMF}}(t)$. The amplitude and phase of two 60-bit mismatched filters are displayed. The subsequent processes follow those shown in (c), resulting in $m_{\mathrm{dp}}(t,i)$ where PSL > PCCL. The final demodulated signal only reflects perturbation without crosstalk.

The first term of (6) represents the result of the i-th code passing through its corresponding decoder $m_{\mathrm{d}}^{i}(t)$, which we refer to as the auto-correlation function; the second term represents the results of other codes passing through the i-th decoder, which we refer to as the cross-correlation function. Here, we emphasize three important points. First, if the peak cross-correlation level (PCCL) of the cross-correlation function is low enough, the second part of (6) can be ignored, leading to a simplification as $m_{\mathrm{dp}}(t,i) \approx m^{i}(t-iT_{\mathrm{rep}}/M) \otimes m_{\mathrm{d}}^{i}(t)$, representing in a low ICC. Second, if the peak sidelobe level (PSL) of the auto-correlation function is sufficiently low, the first part of (6) can be equivalent to its main lobe, i.e., a single-bit pulse. In this case, Eq. (6) can be further simplified to $m_{\mathrm{dp}}(t,i) = \mathrm{main}\{m^{i}(t-iT_{\mathrm{rep}}/M) \otimes m_{\mathrm{d}}^{i}(t)\}$, where $\mathrm{main}\{\cdot\}$ means the main lobe of the function. Third, denoting $\overrightarrow{R_a}$ as the convolution of the auto-correlation function and $h(t)$, which represents the RBS of the i-th code; and $\overrightarrow{R_c}$ signifies the convolution of the cross-correlation function and $h(t)$, depicting the mapping of RBS signals from other codes onto the trace of the i-th code; increasing the ratio of $\mid \overrightarrow{R_a} \mid / \mid \overrightarrow{R_c} \mid$ aids in reducing ICC [27], implies that enlarging the difference between PSL and PCCL can further suppress ICC (more details about the ICC can be found in Appendix A).

The majority of existing OPC methods rely on MF for decoding, where the matched window corresponds to the code itself [28–32]. MF is also employed for decoding the coded reflection signals in OCM-based QDAS [23–25]. Figure 3(c) illustrates the process of decoding RBS traces with MF. Firstly, let the code itself be its decoder, $m_{\mathrm{MF}}(t)$ is obtained by (2). Secondly, the normalized curve of $m_{\mathrm{dp}}(t,i)$ is accessed by applying (6), where $i=1$, the left part of the curve signifies the auto-correlation function, while the right part denotes the cross-correlation function, both having consistent PSL and PCCL. Thirdly, the decoded RBS trace corresponding to the i-th code, i.e., $E'(t,i)$, is obtained by (5). It is noteworthy that the fading of RBS traces causes distortion in the polyphase code, increasing the PSL and PCCL of $m_{\mathrm{dp}}(t,i)$ and deteriorating the orthogonality of codes. Consequently, the second term of (6) becomes non-negligible, leading to a severe ICC in $E'(t,i)$ as shown in Figure 3(c). This underscores the infeasibility of employing the MF for decoding the orthogonal coded RBS traces in DAS. To achieve

CCM in DAS, two concurrent conditions are imperative: (1) employing effective strategies to diminish the PCCL of orthogonal codes, fortifying the orthogonality amid diverse sets of codes, and suppressing ICC; (2) ensuring the PSL remains sufficiently low to avoid changing spatial resolution.

2.2 Inter-channel crosstalk mitigation

Due to the degradation of PSL and PCCL in orthogonal codes caused by RBS fading, the ICC cannot be eliminated by MF. To further mitigate the ICC, mismatched filtering (MMF) [33] is introduced in this work, achieving lower PSL and PCCL by increasing the length of each filter. The following part is the detailed derivation of the mismatched filter bank based on convex optimization, which can be referred to [34, 35].

Let $\boldsymbol{S}$ be the coding sequence set mentioned above, and all the sequences in $\boldsymbol{S}$ can be expressed as $\boldsymbol{s}^i = [s^i(1)s^i(2)\cdots s^i(N)]^{\mathrm{T}}$, where $[\cdot]^{\mathrm{T}}$ denotes the transposition operation. Let $\boldsymbol{U}$ be a mismatched filter bank with a filter length of P ($P \geqslant N$) and filter number of M, which is associated with $\boldsymbol{S}$, and all the filters in $\boldsymbol{U}$ can be defined as $\boldsymbol{u}^i = [u^i(1)u^i(2)\cdots u^i(P)]^{\mathrm{T}}$. Then, for simplification of subsequent calculations and without any loss of generality, $\boldsymbol{s}^i$ is normalized and expanded to

$$\begin{aligned}\boldsymbol{x}^i &= [\ \overbrace{0\cdots 0}^{(P-N)/2}\ s^i(1)s^i(2)\cdots s^i(N)\ \overbrace{0\cdots 0}^{(P-N)/2}\ ]^{\mathrm{T}} / \left\|\boldsymbol{s}^i\right\|_2 \\ &= [x^i(1)x^i(2)\cdots x^i(N)\cdots x^i(P)]^{\mathrm{T}} / \left\|\boldsymbol{s}^i\right\|_2, \quad i = 1, 2, \ldots, M,\end{aligned} \tag{7}$$

where $\|\cdot\|_2$ denotes the Euclidean norm. It should be noted that P needs to be carefully chosen to make sure $(P-N)/2$ is always an integer. Define a matrix $\boldsymbol{X}^i$ of size $P \times (2P-1)$:

$$\boldsymbol{X}^i = \begin{bmatrix} 0 & 0 & \cdots & x^i(1) & x^i(2) & \cdots & x^i(P) \\ 0 & \cdots & x^i(1) & x^i(2) & \cdots & x^i(P) & 0 \\ \vdots & \vdots & \vdots & \vdots & \vdots & \vdots & \vdots \\ 0 & x^i(1) & x^i(2) & \cdots & x^i(P) & \cdots & 0 \\ x^i(1) & x^i(2) & \cdots & x^i(P) & 0 & \cdots & 0 \end{bmatrix}, \tag{8}$$

where $\boldsymbol{X}^i$ is the Hankel matrix of the code vector $\boldsymbol{x}^i$. Remove the P-th column of $\boldsymbol{X}^i$ to obtain a $P \times (2P-2)$ computation auxiliary matrix $\boldsymbol{A}^i$. Then, the PSL of the correlation function between the i-th code vector and the i-th mismatched filter vector can be defined as

$$\mathrm{PSL}_i = \left\|\left(\boldsymbol{A}^i\right)^{\mathrm{H}} \boldsymbol{u}^i\right\|_{\infty}, \tag{9}$$

where $(\cdot)^{\mathrm{H}}$ denotes the conjugate transpose, and $\|\cdot\|_{\infty}$ denotes the maximum norm. Similarly, the PCCL between the i-th mismatched filter vector and the j-th ($j \neq i$) code vector is calculated as

$$\mathrm{PCCL}_i = \left\|\left(\boldsymbol{X}^j\right)^{\mathrm{H}} \boldsymbol{u}^i\right\|_{\infty}. \tag{10}$$

Finally, define a weighting factor w to achieve a good balance between the PSL and PCCL of system, where the system's PSL and PCCL represent the maximum values of PSL_i and PCCL_i ($i = 1, 2, \ldots, M$), respectively. All three parameters are expressed in decibels (dB). To avoid the trivial solutions $\boldsymbol{u}^i = 0$ and without loss of generality, let the peak responses be denoted as $(\boldsymbol{u}^i)^{\mathrm{H}}\boldsymbol{x}^i = 1$. Then, the problem of solving the mismatched filter bank U for the orthogonal codes S can be transformed into the following convex optimization problem:

$$\begin{aligned} &\min_{\boldsymbol{u}^i} \left\{\max\left\{w \cdot \max\left\{\mathrm{PSL}_i\right\}, \max\left\{\mathrm{PCCL}_i\right\}\right\}\right\} \\ &\qquad \text{s.t.} \quad (\boldsymbol{u}^i)^{\mathrm{H}}\boldsymbol{x}^i = 1, \\ &\qquad\qquad\ \text{for } i = 1, 2, \ldots, M, \end{aligned} \tag{11}$$

where $w > 0$ indicates PSL $<$ PCCL, and $w \leqslant 0$ indicates PSL $\geqslant$ PCCL. Note that w has a balancing effect on PSL and PCCL only within a certain range of values [35]. In this work, setting $w \leqslant 0$ is employed

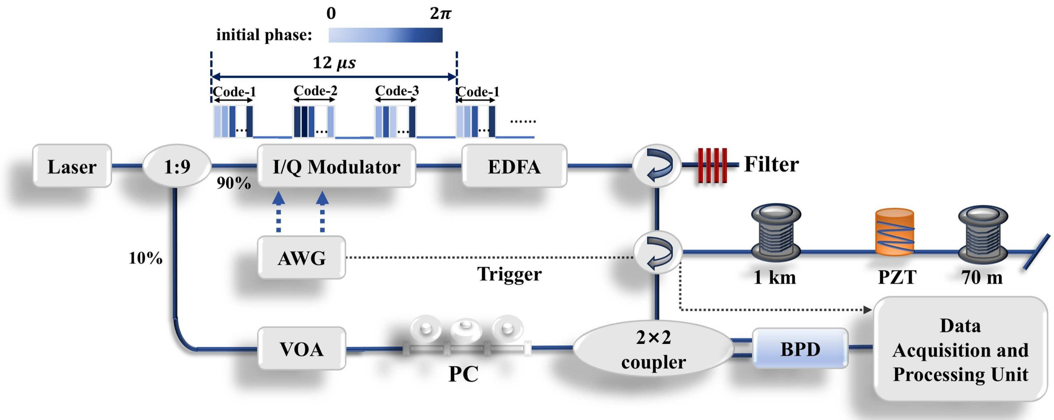

Figure 4 (Color online) Experimental setup.

to achieve lower PCCL and better ICC suppression. Additionally, by adjusting w, PSL can be controlled without affecting spatial resolution. The problem in (11) represents a typical convex optimization problem and can be solved by utilizing the CVX tool [36].

So far, the dedicated mismatched filter $\boldsymbol{u}^i$ for the i-th orthogonal code is devised. Figure 3(d) delineates the process of decoding the coded RBS trace with MMF. Initially, the designed mismatched filter $\boldsymbol{u}^i$ is fed into (4) to derive $m_{\mathrm{MMF}}(t)$, and the amplitude and phase of $\boldsymbol{u}^i$ with 60-bit length are shown in Figure 3(d). Subsequently, by substituting $m_{\mathrm{MMF}}(t)$ into (6), the $m_{\mathrm{dp}}(t,i) \approx m^i(t - iT_{\mathrm{rep}}/M) \otimes m^i_{\mathrm{MMF}}(t)$ is achieved, given that the PCCL here is low enough. Then, substitute $m_{\mathrm{dp}}(t,i)$ into (5) to obtain the decoded RBS trace corresponding to the i-th orthogonal code. Note that PSL is larger than PCCL here, indicating an increase in $|\overrightarrow{R_a}| / |\overrightarrow{R_c}|$ and further decrease of ICC. Finally, an ICC-free demodulation result is successfully attained by fading elimination with the rotated-vector-sum (RVS) method [37] and the sub-chirp-pulse extraction algorithm (SPEA) method proposed by our research group [38]. Importantly, the fading suppression algorithm operates independently of the MMF, ensuring no mutual interference between the two. Additionally, it is worth emphasizing that the proposed scheme focuses solely on pulse coding and decoding within optical fiber sensing systems, making it versatile and widely applicable regardless of whether the sensing mechanism is scattering-based or reflection-based.

3 Experiment and analysis

To verify and demonstrate the practical performance of the proposed scheme, the details of implementing CCM in DAS are provided in this section. It showcases the achievement of CCM-DAS with low ICC through orthogonal coding and MMF decoding, along with its outstanding sensing performance.

3.1 Experimental setup

The experimental setup implemented for the CCM-DAS is shown in Figure 4, a heterodyne detection scheme. The continuous lightwave (CW) from the 1550 nm ultra-narrow linewidth laser is split into two branches via a $1:9$ coupler. The 90% of the light is modulated by the I/Q modulator into a coded probe pulse with 3 sets of orthogonal polyphase codes in the same frequency band. Consistent with the simulation settings (more details can be seen in Appendix B and Table D1 of Appendix D), the duration of each bit is set to 8 ns, and the length of each set is 20-bit, resulting in a 160 ns duration per set. Simultaneously, the time interval between each pair of adjacent sets is 4 μs, and the repetition time for the coded probe pulse is 12 μs.

The I/Q modulator is driven by the coded pulse $m(t)$ generated by the arbitrary waveform generator (AWG). Then, the coded probe pulse is amplified by the erbium-doped fiber amplifier (EDFA) and subsequently passes through a filter for the elimination of the amplified spontaneous emission (ASE) noise generated during amplification. The amplified pulse is then pumped into a 1 km FUT. The piezoelectric ceramic transducer (PZT) wrapped with 12.3-m SMF is applied to generate perturbations. The remaining 10% of the light acts as the local oscillator (LO), beating with the RBS signal from the FUT. The variable optical attenuator (VOA) is employed to regulate the optical power, ensuring that the resultant beat signal

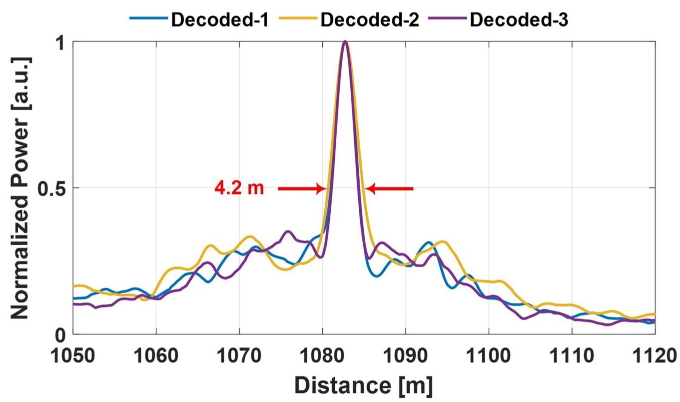

Figure 5 (Color online) Fresnel reflection peak at the end of the decoded and fading eliminated RBS traces. Decoded-i represents the RBS traces corresponding to different orthogonal codes. The FWHM of the Fresnel reflection peaks indicates the experimental system's ideal spatial resolution of 4.2 m.

remains within the operational power threshold of subsequent components. The polarization controller (PC) is utilized to modify the polarization state of the LO light to suppress polarization fading and enhance the quality of the RBS traces. Then, the two lights are combined and beat with each other in a 2×2 coupler and detected by a 1.6 GHz balanced photodetector (BPD). Then detected RBS traces are sampled by an oscilloscope (OSC) at a sampling rate of 5 GSa/s.

During the demodulation process, the designed mismatched filters with a 60-bit length per set are used for decoding first. The value of the weighting factor w is set to -9 dB, and the parameters of MMF here are consistent with those set in the simulation (the amplitudes and phases of these filters can be seen in Tables D2 and D3 of Appendix D). Post-MMF decoding, the pulse width is restored to a single-bit width of 8 ns, which allows the system's spatial resolution to match that of an 8 ns chirp pulse. However, the existence of interference fading complicates the accurate demodulation of disturbance signals. To address this, the SPEA and RVS methods are employed to eliminate fading in the decoded RBS traces, albeit at the cost of degraded spatial resolution. Following phase demodulation, the external vibrations along the FUT can be extracted. Figure 5 illustrates the Fresnel reflection peaks at the end of the decoded and fading eliminated RBS traces, which are associated with the 3 sets of codes in the experiment. The full width at half maximum (FWHM) denotes the theoretical spatial resolution of 4.2 m in the experiment, closely aligning with that in Figure B2 of Appendix B. Notably, the procedures of signal decoding and demodulation remain consistent between the simulation and experiment. Similar to the simulation in Appendix B, to ensure the quality of the experimental demodulated signals, the gauge length (GL) is set to 7.5 m.

3.2 Experimental results

To demonstrate the sensing performance of the CCM-DAS system, a 3 kHz sinusoidal disturbance demodulation test is carried out. Decoding is conducted using both MF and MMF methods for comparison. The resulting differential phase time-distance domain maps are depicted in Figures 6(a) and (b), respectively. Similar to that observed in the simulation (see Figure B3(a) of Appendix B), significant ICCs are observed near 200 and 600 m in Figure 6(a) when using MF decoding (the areas where ICC signals occur can be referred to (B2) of Appendix B). In contrast, Figure 6(b) illustrates that MMF decoding reveals a significant signal only at the end of 1 km fiber, with minimal ICC observed elsewhere, aligning with expectations. According to previous analysis, the magnitude of ICC is solely dependent on the coding and decoding process and is unrelated to the location of the disturbance. Furthermore, when external disturbances are minor, the ICC ceases to exist as it becomes completely submerged in the background noise. Figure 6(c) displays the variance of the differential phase along the fiber, with a rising edge of 7.5 m, matching the anticipated spatial resolution. It is important to note that despite the perturbation phase significantly surpassing the ICCs, complete crosstalk elimination has not been achieved. Further in-depth research is required to devise more effective crosstalk mitigation strategies. Additionally, the time-domain waveform of the disturbance signal is accurately demodulated, as shown in Figure 6(d). Its power spectral density (PSD), depicted by the red curve in Figure 7(a), exhibits harmonics akin to that

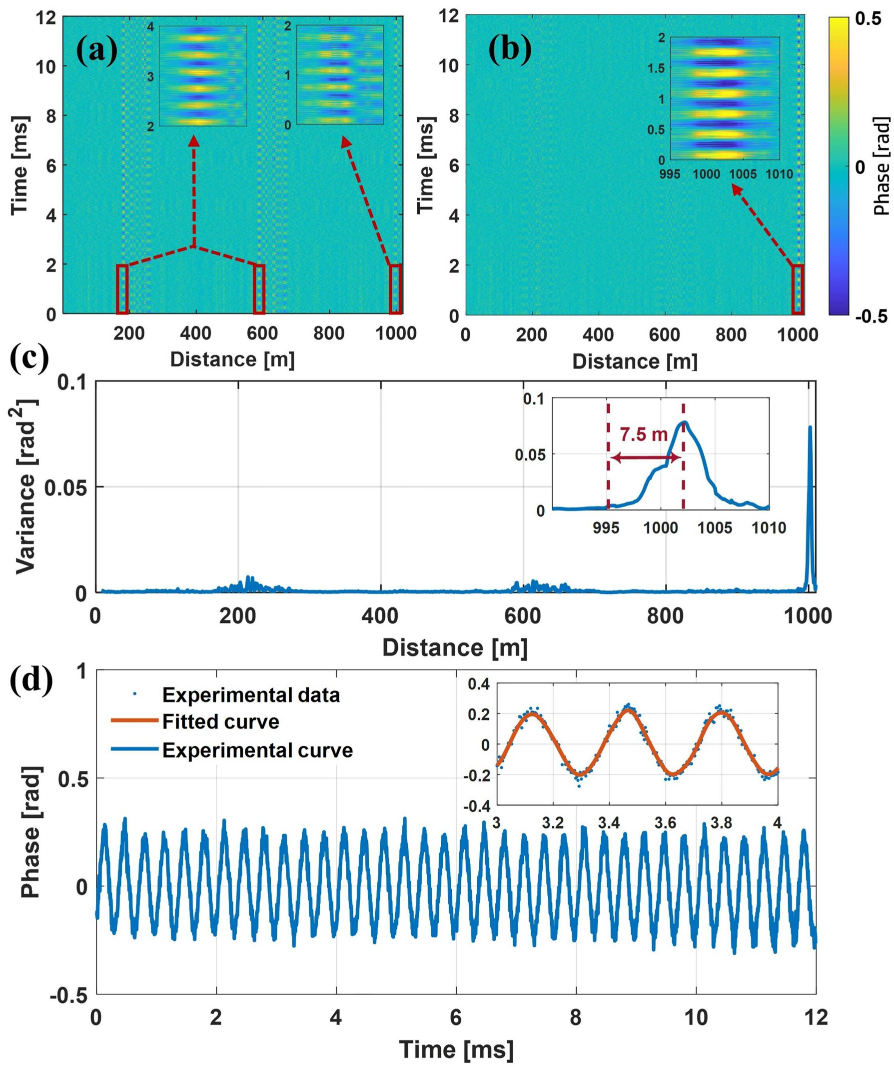

Figure 6 (Color online) Experimental demodulated results. Time-distance domain maps of the differential phase decoded by (a) MF and (b) MMF; (c) the variance of the differential phase along the fiber; (d) time-domain waveform of the demodulated 3 kHz sinusoidal signal.

in Figure B3(d) (see details in Appendix B), but with markedly low peak values that can be considered negligible.

As a kind of OPC technology, this approach can also achieve a higher SNR compared to the conventional single-pulse scheme, which is related to the system's coding gain. To substantiate this claim, the demodulated results of the single-pulse scheme and the coded-pulse scheme for the same disturbance are fairly compared. The single pulse used in the traditional scheme is a chirp pulse with 8 ns duration, consistent with the one-bit LFM pulse parameters in the proposed scheme. A 3 kHz sinusoidal signal is applied to the PZT as an external perturbation. Both schemes employ the same demodulation method, and the PSDs of the demodulated signal are shown in Figure 7(a), where the blue curve presents the result of the traditional single chirp pulse scheme and the red curve represents the result of the proposed coded-pulse scheme. The mean noise level of the coded-pulse scheme is significantly lower than that of the traditional scheme by 18 dB, indicating a substantial improvement in the SNR of the demodulated signal, attributable to the coding gain of CCM-DAS (the theoretical derivation of coding gain can be seen in (C1)–(C6) of Appendix C). This underscores the superior signal demodulation capability of the proposed scheme. Additionally, it is evident that the detectable frequency range of the proposed scheme is three times wider than that of the traditional scheme, implying an enhancement in sensing bandwidth. This will be substantiated in the subsequent discussion.

According to the Nyquist sampling theorem, the response bandwidth of a traditional single-pulse

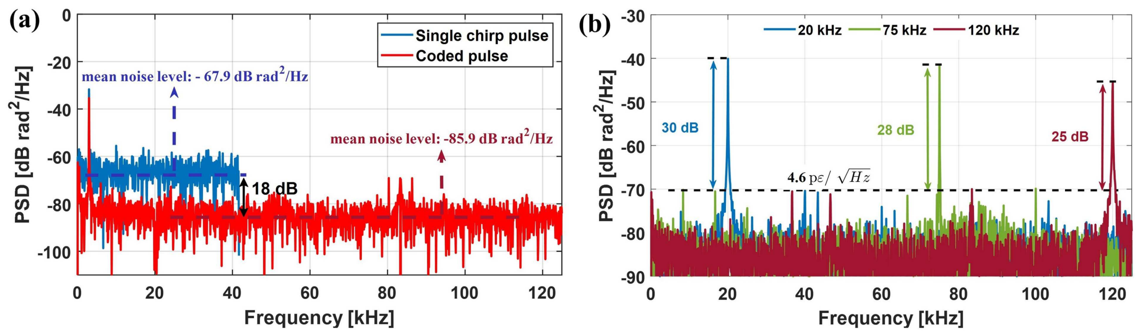

Figure 7 (Color online) (a) Mean noise levels of single chirp pulse and coded pulse sequence scheme (3 sets of orthogonal codes). The PSD plots of the demodulated 3 kHz sinusoidal disturbance are shown for the single chirp pulse (8 ns) scheme (blue curve) and the CCM-DAS scheme with three sets of orthogonal codes (red curve). The mean noise level of the PSD for the single chirp pulse scheme is -67.9 dB rad^2/Hz, while the mean noise level for the CCM-DAS scheme is -85.9 dB rad^2/Hz, representing an SNR improvement of approximately 18 dB. (b) The PSDs of different frequency disturbances. The PSD results of 20 kHz (blue), 75 kHz (green), and 120 kHz (red) sinusoidal disturbances show that the minimum difference between the signal peak and noise level is approximately 25 dB, with the maximum noise level being 4.6 p$\varepsilon/\sqrt{\text{Hz}}$.

scheme with a 12 μs repetition time is 41.6 kHz. Through CCM, the response bandwidth of the proposed scheme increases threefold compared to the traditional scheme, reaching 125 kHz. To evaluate the enhanced response bandwidth capability of the proposed scheme, sinusoidal signals with frequencies of 20 kHz, 75 kHz, and 120 kHz, each with equal amplitudes, are applied to the PZT. Figure 7(b) illustrates the PSDs of the demodulated signals, where the minimum difference between signal peak and noise level is approximately 25 dB, and the maximum noise level is -70 dB rad^2/Hz, corresponding to a strain noise level of 4.6 p$\varepsilon/\sqrt{\text{Hz}}$ according to [39]. This demonstrates the system's robust sensing capability of the proposed scheme in ultra-wideband signal sensing scenarios.

3.3 Longer distance sensing evaluation

Measuring the sensing capability of an optical sensing system at a long distance is a critical metric. The sensing performance of CCM-DAS at a sensing distance of 10 km is demonstrated through experimental results here. The SMF is replaced to a 10 km SMF. Long-distance sensing requires higher pulse energy, hence, the length of each set of the 3 orthogonal codes is increased to 32-bit (the phases of these codes can be found in Table D4 of Appendix D), while maintaining a width of 8 ns per bit. The repetition period of the probe pulse is set to 100.8 μs, corresponding to an approximate detection frequency limit of 4.96 kHz, and the interval between two adjacent codes is 33.6 μs. The length of each mismatched filter is set to 64-bit (the amplitudes and phases of these filters can be seen in Tables D5 and D6 of Appendix D), with w being -9 dB. To ensure data acquisition, the sampling rate of OSC is configured at 2.5 GSa/s, with a sampling time of 32 ms.

In the experiment, a 2 kHz sine disturbance is applied to the PZT, and its phase-distance demodulated result is illustrated in Figure 8(a), which reveals that ICC is submerged in the background noise. The PSD of the demodulated signal is depicted in Figure 8(b), exhibiting an SNR of 24 dB. Further, a chirp signal ranging from 100 Hz to 14.5 kHz is applied to the PZT. The time-domain representation of this chirped disturbance is captured in Figure 8(c), while the short-time Fourier transform (STFT) spectrum is depicted in Figure 8(d), providing a comprehensive view of the signal's frequency characteristic over time. The results depicted in Figure 8 not only underscore the commendable demodulation capabilities of the proposed scheme but also highlight the significant enhancement in bandwidth, which is crucial for long-range applications. These findings underscore the potential of our approach to extend the response bandwidth, offering promising prospects for long-distance distributed broadband detection scenarios and underlining the substantial applicability of our method.

4 Discussion

This study introduces a pioneering CCM scheme for RSISs, fundamentally advancing overall system performance. We validated the feasibility of the CCM approach using the implementation of the DAS system, achieving what we term CCM-DAS. For the first time, our approach harnesses the power of orthogonal

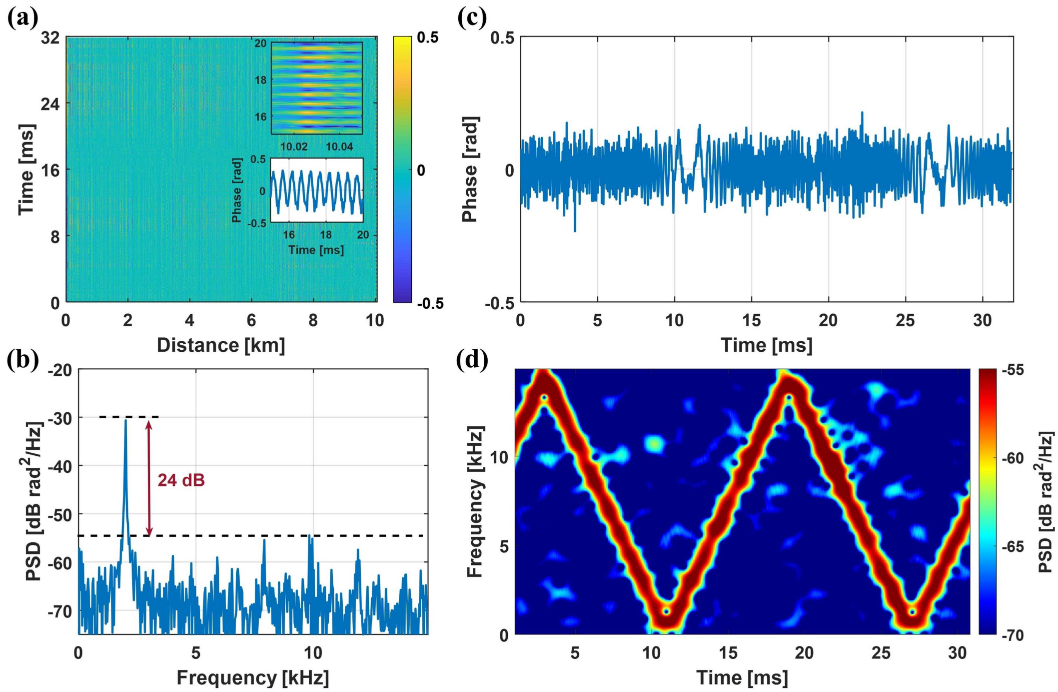

Figure 8 (Color online) Demodulation results of a 10 km sensing distance. (a) The phase-distance map and (b) the PSD of the 2 kHz disturbance signal; (c) the time domain curve and (d) the short-time Fourier transform spectrum of chirped disturbance from 100 Hz to 14.5 kHz.

coding to achieve efficient multiplexing of channels within a single frequency band, to the best of our knowledge. This innovation is further strengthened by the strategic application of mismatched filters, meticulously designed to effectively reduce sidelobe suppression ratios and eliminate ICC. As a result, our technique enables the precise differentiation of overlapping signals within a shared frequency band, a task previously thought infeasible. This marks a substantial departure from traditional channel-multiplexed DAS systems [17–20], which rely on distinct frequency bands for channel multiplexing. Moreover, the number of multiplexed channels in CCM-DAS is not theoretically limited by the system's available bandwidth.

The theoretical underpinnings of our CCM-DAS scheme are meticulously laid out and substantiated through rigorous analysis. Table 1 highlights the overall advantages of the proposed scheme compared to traditional single-pulse and standard OPC approaches. First, taking the traditional single-pulse scheme as a baseline: assuming the fiber length remains constant, the required round-trip time of the probe pulse (i.e., the repetition period) to prevent signal aliasing in the traditional single-pulse scheme with a pulse width T_{d} is denoted as T_{rep}, corresponding to a response bandwidth of $1/2T_{\mathrm{rep}}$. For generality and ease of comparison, we set the coding gain to 1. Next, due to the varying coding schemes employed by different OPC methods [30, 32, 40, 41], the amount of information required for decoding differs, leading to variations in the time needed to complete a single measurement (i.e., a unipolar Golay code with a coding length of N requires $4T_{\mathrm{rep}}$ of measurement information for one decoding, resulting in a measurement time of $4T_{\mathrm{rep}}$ and a corresponding response bandwidth of $1/8T_{\mathrm{rep}}$, with a coding gain (i.e., SNR improvement) of $\sqrt{N}/2$ [41]).

In contrast, CCM-DAS can inject M sets of coded pulses into the fiber within a single repetition period, with each decoding requiring only the measurement information from that period. The resulting improvements in response bandwidth and SNR over the traditional single-pulse scheme are shown in the rightmost column of Table 1, highlighting the significant advantages of our approach (the theoretical derivation of SNR improvement can be seen in (C1)–(C6) of Appendix C). The proof-of-concept experiments that followed not only strongly validate our theoretical assertions but also clearly demonstrate the exceptional sensing capabilities of the proposed system. Notably, the CCM-DAS system delivers a strain noise level that is significantly lowered, all the while achieving an 18 dB increase in SNR compared to the traditional single-pulse scheme. Pushing the boundaries further, the 10 km sensing experiment has yielded a nearly 15 kHz response bandwidth, which is a threefold enhancement over the conventional

Table 1 Comparisons of coding gains and response bandwidths. N is the coding length of the OPC scheme. M is the number of coded pulse sets contained within the CCM-DAS system's coded pulse sequence. T_{rep} represents the round-trip time of the probe pulse in a traditional single-pulse scheme for a fiber of a given length, which is slightly longer than the actual fiber length to ensure that no signal aliasing occurs.

Pulse type	Single-pulse	Simplex code [40]	Unipolar Golay code [41]	Bipolar Golay code [32]	Random code [30]	Co-channel multiplexing
Coding gain	1	$\frac{N+1}{2\sqrt{N}}$	$\frac{\sqrt{N}}{2}$	$\sqrt{N}$	$\frac{\sqrt{N}}{2}$	$\sqrt{MN}$
Measurement time	T_{rep}	NT_{rep}	$4T_{\mathrm{rep}}$	$2T_{\mathrm{rep}}$	T_{rep}	T_{rep}
Response bandwidth	$\frac{1}{2T_{\mathrm{rep}}}$	$\frac{1}{2NT_{\mathrm{rep}}}$	$\frac{1}{8T_{\mathrm{rep}}}$	$\frac{1}{4T_{\mathrm{rep}}}$	$\frac{1}{2T_{\mathrm{rep}}}$	$\frac{M}{2T_{\mathrm{rep}}}$

single-channel scheme.

While these results are promising, there remain areas for further optimization in CCM-DAS. Firstly, to maintain superior sensing performance over extended distances, it is crucial to incorporate the Doppler effect, induced by variations in the fiber path, into the encoding-decoding algorithm. Secondly, future work should consider implementing strategies to mitigate the frequency drift of the laser, ensuring consistent system response to low-frequency signals [25, 42]. Finally, while the current coding and decoding algorithms used in CCM-DAS are effective, they may not yet be optimal, which is a common feature shared in most OPC technologies [29–31]. Enhancing the mismatched filter design algorithm could potentially yield better sidelobe suppression ratios and further improve crosstalk suppression [43, 44].

In conclusion, the proposed CCM-DAS framework presents a transformative solution for broadening the response bandwidth in information systems that rely on Rayleigh scattering, paving the way for next-generation sensing technologies. The advancement holds significant potential for wide-ranging applications across various engineering domains that require the high-fidelity detection of wideband signals. The expansive applications include environmental monitoring, climate change studies, and the detection of geological activities.

Acknowledgements This work was supported by National Natural Science Foundation of China (Grant No. 62435002), Ministry of Science and Technology of China (Grant No. DL2023167001L), Sichuan Science and Technology Program (Grant No. 2023YFSY0058), 111 Project (Grant No. B14039), and Sichuan Natural Science Foundation (Grant No. 2023NSFSC0450).

Supporting information Appendixes A–D. The supporting information is available online at info.scichina.com and link.springer.com. The supporting materials are published as submitted, without typesetting or editing. The responsibility for scientific accuracy and content remains entirely with the authors.

References

1 Lenton T M, Abrams J F, Bartsch A, et al. Remotely sensing potential climate change tipping points across scales. Nat Commun, 2024, 15: 343
2 Ceolato R, Bedoya-Velásquez A E, Fossard F, et al. Black carbon aerosol number and mass concentration measurements by picosecond short-range elastic backscatter lidar. Sci Rep, 2022, 12: 8443
3 She C-Y, Friedman J S. Atmospheric Lidar Fundamentals: Laser Light Scattering from Atoms and Linear Molecules. Cambridge: Cambridge University Press, 2022
4 Bjornson E, Sanguinetti L. Rayleigh fading modeling and channel hardening for reconfigurable intelligent surfaces. IEEE Wireless Commun Lett, 2021, 10: 830–834
5 Redding B, Murray J B, Hart J D, et al. Fiber optic computing using distributed feedback. Commun Phys, 2024, 7: 75
6 Tovar P, von der Weid J P, Wang Y, et al. A random optical parametric oscillator. Nat Commun, 2023, 14: 6664
7 Li J, Kim T, Lapusta N, et al. The break of earthquake asperities imaged by distributed acoustic sensing. Nature, 2023, 620: 800–806
8 Sladen A, Rivet D, Ampuero J P, et al. Distributed sensing of earthquakes and ocean-solid Earth interactions on seafloor telecom cables. Nat Commun, 2019, 10: 5777
9 Walter F, Gräff D, Lindner F, et al. Distributed acoustic sensing of microseismic sources and wave propagation in glaciated terrain. Nat Commun, 2020, 11: 2436
10 Hubbard P G, Xu J, Zhang S, et al. Dynamic structural health monitoring of a model wind turbine tower using distributed acoustic sensing (DAS). J Civil Struct Health Monit, 2021, 11: 833–849
11 Wu H, Liu X, Xiao Y, et al. A dynamic time sequence recognition and knowledge mining method based on the hidden Markov models (HMMs) for pipeline safety monitoring with Φ-OTDR. J Lightwave Technol, 2019, 37: 4991–5000
12 Qi Y, Ni L, Ye Z, et al. Replica symmetry breaking in 1D Rayleigh scattering system: theory and validations. Light Sci Appl, 2024, 13: 151
13 He H, Shao L Y, Luo B, et al. Multiple vibrations measurement using phase-sensitive OTDR merged with mach-zehnder interferometer based on frequency division multiplexing. Opt Express, 2016, 24: 4842–4845
14 Zhang Y, Xia L, Cao C, et al. A hybrid single-end-access MZI and Φ-OTDR vibration sensing system with high frequency response. Opt Commun, 2017, 382: 176–181
15 Qu S, Liu Z, Xu Y, et al. Phase sensitive optical time domain reflectometry based on compressive sensing. J Lightwave Technol, 2019, 37: 5766–5772
16 Li S, Xu Y, Feng Y, et al. Broadband vibration signal measurement based on multi-coset sampling in phase-sensitive OTDR system. IEEE Sens J, 2022, 22: 1295–1300
17 Wang Z, Pan Z, Fang Z, et al. Ultra-broadband phase-sensitive optical time-domain reflectometry with a temporally sequenced multi-frequency source. Opt Lett, 2015, 40: 5192–5195
18 Chen D, Liu Q, Fan X, et al. Distributed fiber-optic acoustic sensor with enhanced response bandwidth and high signal-to-noise ratio. J Lightwave Technol, 2017, 35: 2037–2043

19 Yang G, Fan X, Liu Q, et al. Frequency response enhancement of direct-detection phase-sensitive OTDR by using frequency division multiplexing. J Lightwave Technol, 2018, 36: 1197–1203
20 Xiong J, Wang Z, Wu Y, et al. Long-distance distributed acoustic sensing utilizing negative frequency band. Opt Express, 2020, 28: 35844–35856
21 Liu B, He Z S, Zeng J K, et al. Polyphase orthogonal code design for MIMO radar systems. In: Proceedings of the CIE International Conference on Radar, Shanghai, 2006. 1–4
22 Huang Z, Tang B, Zhang S. Sequential optimisation of orthogonal waveforms for MIMO radar. J Eng, 2019, 2019: 7912–7917
23 Jiang J, Xiong J, Wang Z, et al. Quasi-distributed fiber-optic acoustic sensing with MIMO technology. IEEE Int Things J, 2021, 8: 15284–15291
24 Jiang J, Deng Z, Wang Z. Channel-multiplexing for quasi-distributed acoustic sensing with orthogonal codes. Opt Express, 2021, 29: 36828–36839
25 Deng Z, Wan A, Xu R, et al. Quasi-distributed acoustic sensing based on orthogonal codes and empirical mode decomposition. IEEE Sens J, 2023, 23: 24591–24600
26 Lin S, Wang Z, Xiong J, et al. Rayleigh fading suppression in one-dimensional optical scatters. IEEE Access, 2019, 7: 17125–17132
27 Deng Y, Liu Q, Liu S, et al. Multipath quasi-distributed acoustic sensing based on space division multiplexing and time-gated OFDR. IEEE Sens J, 2023, 23: 11615–11620
28 Wang P, Zhang H, Chen J, et al. Ultra-long range distributed acoustic sensor using poly-phase coding approach. J Lightwave Technol, 2024, 42: 2595–2603
29 Wang Z, Zhang B, Xiong J, et al. Distributed acoustic sensing based on pulse-coding phase-sensitive OTDR. IEEE Int Things J, 2019, 6: 6117–6124
30 Li P, Wang Y, Yin K, et al. Random coding method for coherent detection φ-OTDR without optical amplifier. Opt Lasers Eng, 2023, 161: 107318
31 Shiloh L, Levanon N, Eyal A. Highly-sensitive distributed dynamic strain sensing via perfect periodic coherent codes. In: Proceedings of the 26th International Conference on Optical Fiber Sensors, Lausanne, 2018
32 Wu Y, Wang Z, Xiong J, et al. Bipolar-coding Φ-OTDR with interference fading elimination and frequency drift compensation. J Lightwave Technol, 2020, 38: 6121–6128
33 Ackroyd M, Ghani F. Optimum mismatched filters for sidelobe suppression. IEEE Trans Aerosp Electron Syst, 1973, AES-9: 214–218
34 Griep K R, Ritcey J A, Burlingame J J. Poly-phase codes and optimal filters for multiple user ranging. IEEE Trans Aerosp Electron Syst, 1995, 31: 752–767
35 Hu L B, Liu H W, Feng D Z, et al. Optimal mismatched filter bank design for MIMO radar via convex optimization. In: Proceedings of the International Waveform Diversity and Design Conference, Niagara, 2010. 126–131
36 Grant M, Boyd S. CVX: Matlab software for disciplined convex programming, version 2.0 beta. 2013. https://cvxr.com/cvx
37 Chen D, Liu Q, He Z. Phase-detection distributed fiber-optic vibration sensor without fading-noise based on time-gated digital OFDR. Opt Express, 2017, 25: 8315–8325
38 Xiong J, Wang Z, Wu Y, et al. Single-shot COTDR using sub-chirped-pulse extraction algorithm for distributed strain sensing. J Lightwave Technol, 2020, 38: 2028–2036
39 Chen D, Liu Q W, He Z Y. Distributed fiber-optic acoustic sensor with sub-nano strain resolution based on time-gated digital OFDR. In: Proceedings of the Asia Communications and Photonics Conference, Guangzhou, 2017
40 Yu X D, Jing S Z, Zhang Z X, et al. A distributed optical fiber Raman temprature sensor with cyclic simplex coding. Acta Photon Sin, 2014, 43: 706005
41 Nazarathy M, Newton S A, Giffard R P, et al. Real-time long range complementary correlation optical time domain reflectometer. J Lightwave Technol, 1989, 7: 24–38
42 Liu C, Deng Z, Wang Y, et al. Golay coding Φ-OTDR with distributed frequency-drift compensation. IEEE Sens J, 2022, 22: 12894–12899
43 Gao Y, Fan H, Ren L, et al. Joint design of waveform and mismatched filter for interrupted sampling repeater jamming suppression. IEEE Trans Aerosp Electron Syst, 2023, 59: 8037–8050
44 Chatzitheodoridi M E, Taylor A, Rabaste O, et al. A cooperative SAR-communication system using continuous phase modulation codes and mismatched filters. IEEE Trans Geosci Remote Sens, 2023, 61: 1–14